

Protocols for a many-body phase microscope: From coherences and *d*-wave superconductivity to Green's functions

Christof Weitenberg,^{1,*} Luca Asteria,² Ola Carlsson,³ Annabelle Bohrdt,^{3,4} and Fabian Grusdt^{3,4}

¹*Department of Physics, TU Dortmund University, 44227 Dortmund, Germany*

²*Department of Physics, Graduate School of Science, Kyoto University, Kyoto 606-8502, Japan*

³*Department of Physics and Arnold Sommerfeld Center for Theoretical Physics (ASC),
Ludwig-Maximilians-Universität München, 80333 München, Germany*

⁴*Munich Center for Quantum Science and Technology (MCQST), 80799 München, Germany*

(Dated: February 13, 2026)

Quantum gas microscopes probe quantum many-body lattice states via projective measurements in the occupation basis, enabling access to various density and spin correlations. Phase information, however, cannot be directly obtained in these setups. Recent experiments went beyond this by measuring local current operators and local phase fluctuations. Here we propose how Fourier-space manipulation in a matter-wave microscope allows access to various long-range off-diagonal correlators in experimentally realistic settings, realizing a many-body phase microscope. We demonstrate in particular how the fermionic *d*-wave superconducting order parameter in arbitrary Hubbard-type models, the non-equal time Green's function yielding the spectral function, or the hidden order of composite bosons in a fractional Chern insulator can be directly measured. Our results show the great potential of matter-wave microscopy for accessing exotic correlators including phases and coherences and characterizing intriguing quantum many-body states.

I. INTRODUCTION

Ultracold atoms in optical lattices constitute a formidable experimental platform for studying quantum many-body systems due to their tunability and versatile detection schemes. In particular, quantum gas microscopes allow projective measurements of the many-body system with single-site resolution and single-atom sensitivity [1–3] allowing access to density-density correlators [4] and also multi-point spin correlators [5] or string order correlators [4, 6]. Several works proposed protocols for also accessing off-diagonal correlations and coherences [7–12] and recent experiments demonstrated measurements of local currents operators [13, 14] and local phases [15] with single-lattice-site resolution. These measurements ultimately rely on a mapping to density, either mapping local currents to density imbalances using controlled tunneling dynamics in local double wells [13] or mapping local phase fluctuations to density fluctuations via a matter-wave analog of phase contrast imaging [12, 15]. The matter-wave microscope consists of a sequence of time-domain matter-wave lenses formed by quarter-period ($T/4$) evolutions in harmonic traps with a magnification given by the ratio of the trap frequencies [16, 17]. Next to the large magnification up to 93 and high effective resolution without limitation from optical diffraction [16], the method also gives access to Fourier space between the two matter-wave lenses [12]. As we will show here, this unlocks a powerful toolbox for the investigation of many-body quantum systems, through the introduction of highly non-local correlators.

II. MANY-BODY INTERFEROMETER

Here we propose protocols using the matter-wave microscope with Fourier-space manipulation [12, 15] for accessing various non-local off-diagonal correlators in quantum gas microscopes. The idea is based on a many-body interferometer scheme as sketched in Fig. 1. A Raman $\pi/2$ pulse into an auxiliary spin state is applied in Fourier space (i.e., after applying a $T/4$ pulse) and transfers an appropriate momentum \mathbf{q} controlled by the choice of the wave vectors of two Raman beams. The second matter-wave lens realizes another $T/4$ pulse and converts the momentum transfer into a displacement $\mathbf{d}(\mathbf{q})$ in real space [18]. A second Raman pulse without momentum transfer then closes the interferometer sequence and leads to interference between the shifted and unshifted system. The interference fringes in spin-resolved measurements, recorded as a function of the Raman phases, reveal the coherence in the system over the distance given by the chosen shift.

The quantities measured after manipulation by matter-wave lenses and Raman beams can be understood by the corresponding evolution of operators in the Heisenberg picture. We define the creation operator $\hat{a}_{\mathbf{x},\uparrow/\downarrow}^\dagger$ for a fermion or boson at position \mathbf{x} with spin up/down and the operator $\hat{a}_{\mathbf{k},\uparrow/\downarrow}^\dagger$ for the corresponding momentum

$$\hbar\mathbf{k}(\mathbf{x}) = m\omega_1\mathbf{x} \quad (1)$$

determined by the trap frequency ω_1 of the matter-wave lens and the particle mass m . With the initial state polarized to the physical spin \uparrow , a density measurement after closing the interferometer in the fourth step then reads

* christof.weitenberg@tu-dortmund.de

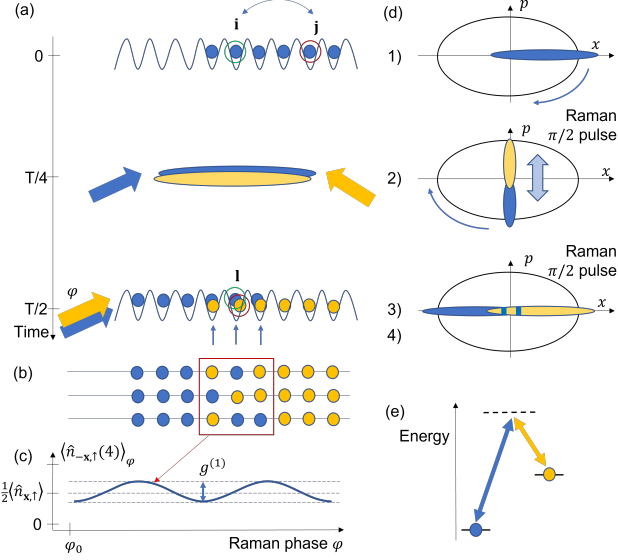


FIG. 1. Proposed protocol for measuring equal-time Green's functions and off-diagonal long-range order. (a) Sketch of the general protocol using a matter-wave microscope. Details are described in the main text. 1) Atoms are initially in an optical lattice in a strongly-correlated regime, all in spin state \uparrow (blue) ($t = 0$). 2) After instantaneously switching off the lattice and interactions, a $T/4$ matter-wave pulse transforms the system into Fourier space, where directly afterwards (at $t = T/4$) a $\pi/2$ Raman pulse brings the system into superposition with an auxiliary spin state \downarrow (yellow) that acquires a momentum kick. 3) After another $T/4$ step, a second $\pi/2$ Raman pulse in the matter-wave image plane (at $t = T/2$) but without momentum transfer makes lattice sites with a given distance $\mathbf{d} = \mathbf{i} - \mathbf{j}$ interfere (note that the matter-wave protocol inverts the image). 4) Spin-resolved single-atom imaging. (b) Example results of snapshot measurements. (c) If there is coherence between sites \mathbf{i} and \mathbf{j} , one expects to see clear fringes in the measured density $\langle \hat{n}_{\mathbf{x},\uparrow}(4) \rangle_\varphi$ of the initial spin state \uparrow as a function of the phase φ of the second Raman pulse. Their amplitude corresponds directly to the $g^{(1)}(\mathbf{d})$ correlation function. The phase offset φ_0 of the fringe (e.g. due to time-reversal symmetry breaking) encodes the complex phase of $g^{(1)}(\mathbf{d})$. (d) Illustration of the protocol in phase space, where $T/4$ pulses swap the roles of x and p , indicating the interferometer scheme. (e) The blue and yellow arrows indicate the utilized Raman transition between the two spin states.

(see Appendix)

$$\begin{aligned} \langle \hat{n}_{-\mathbf{x},\uparrow}(4) \rangle &= \langle \hat{a}_{-\mathbf{x},\uparrow}^\dagger(4) \hat{a}_{-\mathbf{x},\uparrow}(4) \rangle \\ &= \frac{1}{4} [\langle \hat{n}_{\mathbf{x},\uparrow} \rangle + \langle \hat{n}_{\mathbf{x}+\mathbf{d},\uparrow} \rangle - (e^{-i\varphi} \langle \hat{a}_{\mathbf{x}+\mathbf{d},\uparrow}^\dagger \hat{a}_{\mathbf{x},\uparrow} \rangle + \text{h.c.})]. \end{aligned} \quad (2)$$

Expectation values in the second line are evaluated with respect to the original many-body wavefunction before the sequence. This expression contains the interference term between sites separated by distance \mathbf{d} , assumed to be an integer multiple of the lattice constant a_{lat} . If the

system is additionally invariant under time-reversal and translations, the phase coherence function (or equal-time single-particle Green's function)

$$g^{(1)}(\mathbf{d}) = \langle \hat{a}_{\mathbf{x}+\mathbf{d},\uparrow}^\dagger \hat{a}_{\mathbf{x},\uparrow} \rangle \quad (3)$$

is real, and one finds (see Fig. 1 c)

$$\langle \hat{n}_{-\mathbf{x},\uparrow}(4) \rangle = \frac{1}{2} \langle \hat{n}_{\mathbf{x},\uparrow} \rangle - \frac{1}{2} \cos(\varphi) \langle \hat{a}_{\mathbf{x}+\mathbf{d},\uparrow}^\dagger \hat{a}_{\mathbf{x},\uparrow} \rangle. \quad (4)$$

The phase coherence is given by the fringe contrast, which can be obtained by subtracting two measurements where the Raman phase is set to $\varphi = 0$ and $\varphi = \pi$. Evaluating many lattice sites allows extracting average values from a single snapshot. Comparing the mean density in the overlapping region of the system and its shifted copy with the mean density away from the overlap even allows extracting the phase coherence from a single snapshot. In the case when $g^{(1)} \in \mathbb{C}$ is complex, e.g., in the presence of gauge fields, for systems out of equilibrium or with spontaneous symmetry breaking, the fringe will be shifted in φ , and mapping out the signal w.r.t. the interferometer phase φ gives access also to the complex phase of $g^{(1)}$, similar to the phase microscope [15].

The idea discussed above is very general and applies to bosons, fermions and spin-mixtures. It can serve as a powerful building block for far more complex measurement sequences. In the following we discuss several concrete protocols, which access particularly relevant correlators for ongoing quantum simulation efforts. We also discuss experimental considerations at the end of the manuscript.

III. D-WAVE SUPERCONDUCTING ORDER

The question under which conditions the repulsive Fermi-Hubbard model hosts a d -wave superconductor at low temperatures constitutes an urgent quest of quantum-many body physics [19]. Recent progress in the preparation of Fermi-Hubbard systems with ultracold atoms, through new cooling techniques [20] and the entrance of the pseudogap regime [21, 22], pushes these systems towards an answer. The d -wave order parameter can be accessed through the measurement of pairing correlations, i.e., four-point correlators of the form

$$C_{\mu,\nu}(\mathbf{i} - \mathbf{j}) = \langle \hat{a}_{\mathbf{i},\uparrow}^\dagger \hat{a}_{\mathbf{i}+\mathbf{e}_\mu,\uparrow}^\dagger \hat{a}_{\mathbf{j},\downarrow} \hat{a}_{\mathbf{j}+\mathbf{e}_\nu,\downarrow} \rangle \quad (5)$$

including displacements along the unit vectors \mathbf{e}_x and \mathbf{e}_y along the $\mu, \nu = x$ and y directions; here \uparrow, \downarrow correspond to two physical spin states.

Next to the preparation of the d -wave superconductor, accessing its characteristic long-range off-diagonal pairing correlations $C_{\mu,\nu}(\mathbf{d})$ at large \mathbf{d} is a major challenge and so far only few protocols based on noise correlations have been described [23, 24]. The problem becomes easier when leveraging the mapping to an attractive Hubbard model [25], where realistic measurement protocols

for quantum gas microscopes have been identified [26, 27]. However, the mapping from the repulsive to the attractive Hubbard model fails when the diagonal hopping term t' is included, which has been established to play an important role for stabilizing the d -wave phase [28]. Therefore the call for a feasible measurement protocol of d -wave order in the repulsive Fermi Hubbard model is timely.

Here we show that a spinful version of the general protocol introduced in Sec. II allows directly accessing superconducting order in general Hubbard-type models. This is based on the interpretation of $C_{\mu,\nu}(\mathbf{d})$ as a phase coherence function similar to $g^{(1)}(\mathbf{d})$ but formulated for a pair of spins. Thereby the spatial symmetry of the local pair wavefunction is encoded in the dependence on μ and ν and allows to further distinguish between different pairing symmetries. E.g., for an s -wave (d -wave) superconductor $C_{x,y}(\mathbf{d}) = +C_{x,x}(\mathbf{d})$ ($C_{x,y}(\mathbf{d}) = -C_{x,x}(\mathbf{d})$), i.e. bonds along \mathbf{e}_x and \mathbf{e}_y are in (out-of) phase. Our scheme is summarized in Fig. 2 and can be applied e.g. to detect s -wave (d -wave) superconducting order in attractive (repulsive) Hubbard models.

For the measurement of $C_{\mu,\nu}(\mathbf{d})$, we propose to use two auxiliary spin states complementing the two physical spin states. Performing the same interferometry steps as described in Sec. II for the measurement of $g^{(1)}$, but independently between each physical spin and its corresponding auxiliary spin, see Fig. 2 a-b, different displacements $\mathbf{d}_1 = \mathbf{i} - \mathbf{j}$ and $\mathbf{d}_2 = \mathbf{i} - \mathbf{j} + \mathbf{e}_\mu - \mathbf{e}_\nu$ can be independently realized for \uparrow and \downarrow respectively by choosing corresponding momentum kicks of the two Raman pulses. Moreover, the phases of the two Raman pulses, serving as control phases in the Ramsey interferometer, can be independently set to φ_1, φ_2 . By choosing other Raman kicks, pairing correlations involving beyond-nearest neighbor pairs $\sim \hat{a}_{\mathbf{i}\uparrow}^\dagger \hat{a}_{\mathbf{i}+\mathbf{r}\downarrow}^\dagger$ with pair sizes \mathbf{r} involving larger integer multiples of \mathbf{e}_μ would also be accessible. Assuming that the system is invariant under time-reversal, one can show that a combination of four measurements with different Raman phases $\varphi_1 = \varphi_2 = \varphi$ suffices to extract the pairing correlator from density-density correlations obtained in last step of the sequence (see Appendix):

$$\begin{aligned} & \langle \hat{n}_{-\mathbf{j}\uparrow}(4) \hat{n}_{-\mathbf{j}-\mathbf{e}_\nu\downarrow}(4) \rangle_{\varphi=0} + \langle \hat{n}_{-\mathbf{j}\uparrow}(4) \hat{n}_{-\mathbf{j}-\mathbf{e}_\nu\downarrow}(4) \rangle_{\varphi=\pi} \\ & - \langle \hat{n}_{-\mathbf{j}\uparrow}(4) \hat{n}_{-\mathbf{j}-\mathbf{e}_\nu\downarrow}(4) \rangle_{\varphi=\pi/2} - \langle \hat{n}_{-\mathbf{j}\uparrow}(4) \hat{n}_{-\mathbf{j}-\mathbf{e}_\nu\downarrow}(4) \rangle_{\varphi=-\pi/2} \\ & = \frac{1}{2} \langle \hat{a}_{\mathbf{i}\uparrow}^\dagger \hat{a}_{\mathbf{i}+\mathbf{e}_\mu\downarrow}^\dagger \hat{a}_{\mathbf{j}\uparrow} \hat{a}_{\mathbf{j}+\mathbf{e}_\nu\downarrow} \rangle = \frac{1}{2} C_{\mu,\nu}(\mathbf{i} - \mathbf{j}). \end{aligned}$$

Here we assumed fermionic operators $\hat{a}_{\mathbf{j},\sigma}^{(\dagger)}$, although a similar relation can be obtained for bosons.

Computing long-range off-diagonal superconducting correlations $C_{\mu,\nu}(\mathbf{d})$ for ground states of 2D Hubbard models is extremely challenging also numerically. Recent works suggest that with diagonal tunneling t' and at zero temperature, these superconducting correlations drop over a few lattice sites to a constant value of 10^{-4} [19]. The algebraic decay expected for finite temperature will require the detection of signals on a similar level. The signal is expected to be quasi isotropic, such

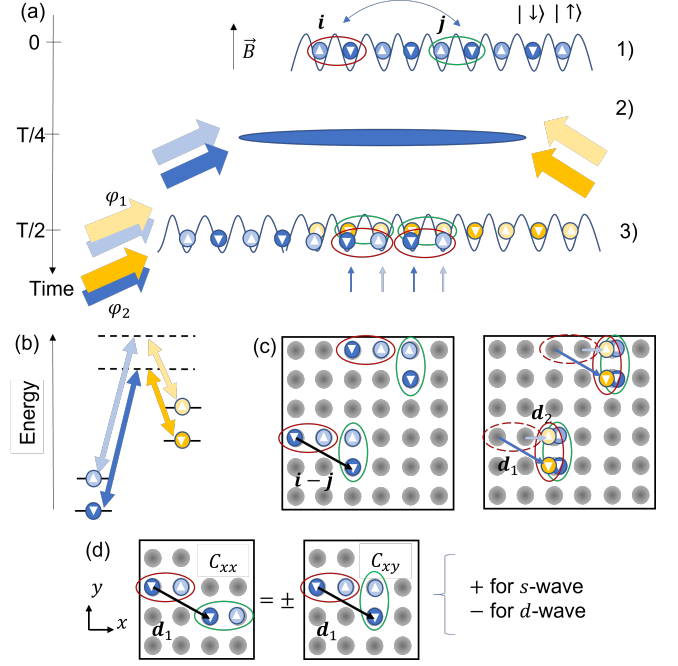


FIG. 2. Proposed protocol for measuring the superconducting orders with arbitrary pairing symmetry. (a) Spinful version of the protocol in Fig. 1 using two physical spins (dark and light blue) and two auxiliary spins (dark and light yellow). Superconducting correlations can be detected from suitable four-point correlators $C_{\mu,\nu}(\mathbf{d})$ (see main text). (b) The four spin states are connected by separate Raman transitions. (c) Protocol for distinguishing between different pairing symmetries. The Raman transition for the spin-up state gives a kick that yields a translation by $\mathbf{d}_1 = \mathbf{i} - \mathbf{j}$ (dark blue arrow), while the spin-down state is translated by $\mathbf{d}_2 = \mathbf{i} - \mathbf{j} + \mathbf{e}_\mu - \mathbf{e}_\nu$ (light blue arrow) – shown here for the combination $\mu = x, \nu = y$. This interferes the wavefunction of a pair of atoms, each displaced along a different direction, with itself at a controlled separation. (d) Illustration of the distinction between s -wave and d -wave superconducting order.

that the correlator corresponding to different $\mathbf{i} - \mathbf{j}$ can be averaged. It is to be expected that resolving the universal part of the correlator will require on the order of 10^4 measurements, but even from the much stronger signal of the non-universal part at shorter distances, one will be able to access the pairing symmetry and to verify the expected d -wave nature of the pairing.

IV. NON-EQUAL-TIME CORRELATIONS AND ARPES SPECTRA

The spectral function $A(\mathbf{k}, \omega) = -\pi^{-1} \text{Im}[G(\mathbf{k}, \omega)]$ is a central concept for understanding quantum many-body systems and their excitations, e.g., for studying mobile dopants in correlated quantum magnets [29–31] or polarons in Bose-Einstein condensates [32, 33]. In solid-state systems, it can be directly accessed via angle-resolved photoemission spectroscopy (ARPES) [34, 35].

Likewise, using Raman pulses [36, 37] or lattice modulations [30, 38] in linear response regime, $A(\mathbf{k}, \omega)$ can be measured in cold atom systems [39] and quantum gas microscopes [29], but obtaining the required statistics in the latter represents a major challenge. In numerical simulations, on the other hand, it is often more convenient to compute the retarded Green's function $G(\mathbf{k}_0, \omega)$ as the Fourier transform of the non-equal-time correlation function $G(\mathbf{k}_0, t) = -i\theta(t)\langle \hat{a}_{\mathbf{k}_0}^\dagger(t)\hat{a}_{\mathbf{k}_0}(0) \rangle$, with the heaviside step function $\theta(t)$ restricting to times $t > 0$. This relation of A and G has also been employed in experimental studies of quantum impurities immersed in a bath [40–42], where Ramsey interferometry can be used to directly measure $G(\mathbf{k}_0, t)$ [8], without a linear response assumption. Obtaining non-equal-time correlation functions with full momentum resolution in bulk many-body systems and without (auxiliary) impurities is a major challenge, however.

Here we propose a suitable protocol for directly measuring the retarded Green's function $G(\mathbf{k}_0, t)$ at a pre-defined momentum \mathbf{k}_0 , based on the matter-wave microscope as summarized in Fig. 3. The idea is to extract a particle in momentum mode \mathbf{k}_0 from the system, by (partially) transferring it to the auxiliary spin state with a $\pi/2$ Ramsey pulse. This can be achieved using a focused Raman beam in Fourier space, i.e. after a $T/4$ pulse. The extracted particle is then kept in spatial isolation while evolving the rest of the many-body system for a duration t . Afterwards, the Ramsey interferometer is closed by returning the extracted particle in a second $\pi/2$ Ramsey pulse. Similar to Fig. 1, the Ramsey scheme gives access to an off-diagonal two-point correlator, but now for operators in a single, well-defined momentum mode \mathbf{k}_0 and at non-equal times.

In the following we discuss a spin-polarized (\uparrow) system coupled to an auxiliary spin state (\downarrow) and refer to Sec. IXD for the generalization to spinful models. In this case, the \uparrow density measured after completing the final, sixth step of the sequence described above at position $-\mathbf{x}_0$, corresponding to the target momentum \mathbf{k}_0 in Fourier space, reads (see Appendix for a detailed derivation):

$$\langle \hat{n}_{-\mathbf{x}_0\uparrow}(6) \rangle = \frac{1}{2} \langle \hat{n}_{\mathbf{k}_0\uparrow} \rangle - \frac{1}{4} \left(e^{-i\varphi - i\varepsilon_{\mathbf{k}_0} t} \langle \hat{a}_{\mathbf{k}_0\uparrow}^\dagger(t) \hat{a}_{\mathbf{k}_0\uparrow}(0) \rangle + \text{h.c.} \right), \quad (6)$$

where the right-hand side of the equation is evaluated with respect to the original many-body wavefunction from the start of the sequence. As the non-equal time correlators are generally complex, the fringe contrast must be mapped out over φ to extract the phase of the correlator, $\varphi_0 = \arg \langle \hat{a}_{\mathbf{k}_0\uparrow}^\dagger(t) \hat{a}_{\mathbf{k}_0\uparrow}(0) \rangle$, as sketched in Fig. 1(c).

The selected momentum mode \mathbf{k}_0 is spatially isolated from the system during the many-body time evolution, as illustrated in Fig. 3. As it typically contains one atom or less, interactions in this mode can be neglected. Further, since the momentum mode is an eigenstate of the lattice,

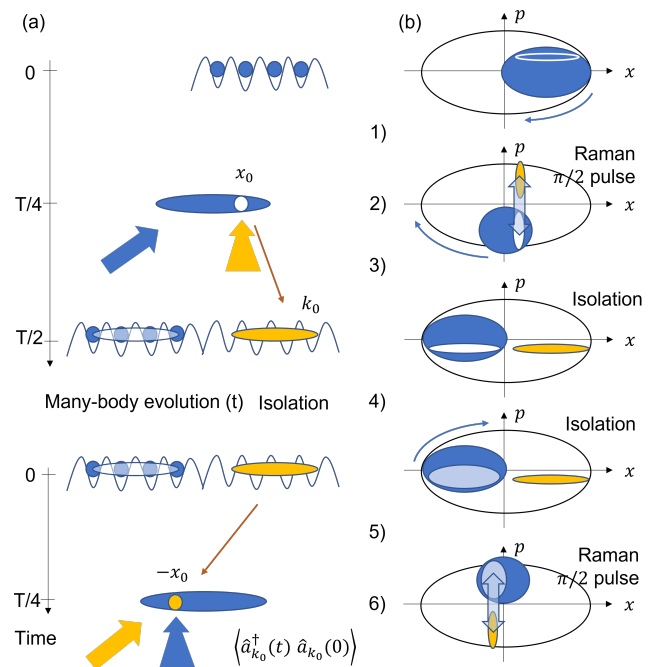


FIG. 3. Proposed protocol for measuring non-equal time correlators. (a) 1) A strongly correlated system is initialized, interactions and lattice potentials are switched off, and a $T/4$ pulse takes it into the Fourier plane. 2) A $\pi/2$ Ramsey pulse with one focused Raman beam at \mathbf{x}_0 extracts a particle in a selected momentum mode $\mathbf{k}_0(\mathbf{x}_0)$, see Eq. (1). 3) In the image plane (at $T/2$) this mode is shifted and therefore isolated from the remaining many-body system, which 4) undergoes its intrinsic many-body dynamics after reloading into the original lattice and switching on interactions. The extracted momentum mode is indicated by the white hole in the system. 5) In a second Fourier plane (after applying another $T/4$ pulse), the selected momentum mode is brought to interference with the system via 6) a second $\pi/2$ Raman pulse giving access to the correlator $\langle \hat{a}_{\mathbf{k}_0\uparrow}^\dagger(t) \hat{a}_{\mathbf{k}_0\uparrow}(0) \rangle$ (see main text). (b) Illustration of the protocol in phase space in order to showcase the interferometer sequence.

it does not disperse during the many-body time-evolution in the middle of the sequence (see Sec. VI for further discussion). It only undergoes a dynamical phase evolution $e^{-i\varepsilon_{\mathbf{k}_0} t}$ resulting from the single-particle band structure $\varepsilon_{\mathbf{k}_0}$, which can be calibrated independently, e.g., by a non-interacting reference measurement, and needs to be subtracted from the measured phase of the fringe. In contrast, the many-body system with a particle removed from momentum mode \mathbf{k}_0 is no longer an eigenstate of the full many-body Hamiltonian, and its non-trivial time evolution leads to the reduced amplitude in the interference, which produces the desired signal in $G(\mathbf{k}_0, t)$.

As in the previous protocols (Secs. II–III) the present scheme involves instantaneously turning off interactions as a first step. However, additional care must be taken with the lattice potential, as the original quasimomentum modes need to eventually be transferred back into the lattice to undergo many-body time-evolution. Instead of

instantaneously switching off the lattice, this demands a controlled band mapping (with interactions switched off): By adiabatically lowering the lattice, each quasimomentum state κ is transferred into one well-defined momentum state \mathbf{k} of the continuum. Subsequently the desired momentum \mathbf{k}_0 can be targeted locally at \mathbf{x}_0 in the Fourier plane. Following the interferometry steps in the matter wave microscope, the lattice can be raised again using inverse band mapping, affecting both the many-body system and the outcoupled, i.e. spatially isolated, particle. The latter has a well-defined quasimomentum κ_0 in the lattice, and the rest of the many-body system transfers to the initial state, albeit with one particle removed in the target quasimomentum mode κ_0 . Crucially, during band mapping, each single-particle quasimomentum mode κ picks up a dynamical phase $\phi(\kappa)$, which needs to be compensated in order to coherently restore the system before it can undergo the many-body time evolution. This can be achieved by imprinting a suitable phase in the matter-wave Fourier plane at time $T/4$.

Alternatively, instantaneous ramping of the lattice can still be performed, if some additional precautions are taken. This will identify every occupied quasimomentum state κ in the first Brillouin zone (BZ) of the lattice not with a single momentum in the continuum, but a superposition of momenta $\mathbf{k}_n = \kappa + \sum_{\mu} n_{\mu} \mathbf{K}_{\mu}$ (with weights $u_n(\kappa)$) interspersed by reciprocal lattice vectors \mathbf{K}_{μ} , with $\mu = x, y, \dots$ and $n_{\mu} \in \mathbb{Z}$. The (continuum) mode \mathbf{k}_0 within the BZ, selected in the Fourier plane at $T/4$, therefore only targets extraction of a particle in component $\mathbf{n} = 0$ while weight from higher momenta $\mathbf{n} \neq 0$ are not targeted. This corresponds to attempting extraction also of higher bands of the quasimomentum spectrum, but since only the lowest band is assumed occupied in the initial state the signal is simply reduced by a factor $|u_0(\kappa)|^2$. The fate of the isolated momentum mode demands some attention however, as loading it instantaneously into the lattice will lead to umklapp processes and non-trivial time evolution. This could be circumvented e.g. by loading it into an auxiliary harmonic trap away from the bulk lattice system, where revolutions in a matter wave lens can impart trivial time evolution for this leg of the interferometer.

While spectroscopy relies on the linear-response regime for accessing the spectral function, which requires compromises with the signal strength, this real-time approach avoids this limitation and should allow for measurements with good signal and high spectral resolution.

V. HIDDEN OFF-DIAGONAL ORDER

Another topic at the focus of cold atom quantum simulation efforts are topological phases, which feature intriguing properties such as topologically protected excitations. Recent work with cold atoms in optical potentials has realized minimal versions of two interacting bosons [43] and two interacting fermions [44], but for

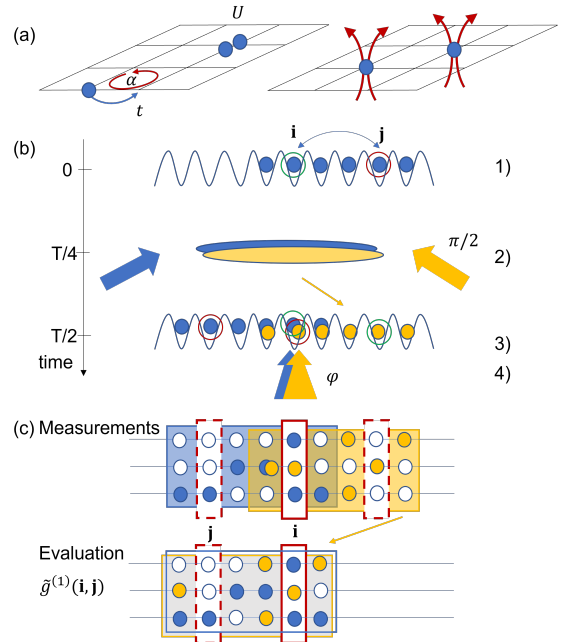


FIG. 4. Measuring hidden off-diagonal long-range order in fractional quantum Hall systems. (a) 2D lattice with magnetic flux α and on-site interaction U , which gives rise to fractional quantum Hall phases for suitable parameters (left). Such systems can be described by composite bosons by attaching magnetic flux tubes (right). (b) Proposed protocol for measuring off-diagonal long-range correlations of composite bosons. 1)-4) the steps are as in Fig. 1, but the second Raman pulse in step 3) is only locally applied via tweezers through a microscope. (c) For the evaluation, the measurements of the auxiliary spin (yellow) are shifted back to obtain the total density (each row is a cut through the 2D system), except for the two sites i, j connected by the focused Raman beam (red box), where the coherence is evaluated from the spin contrast. The data in the dashed red boxes does not enter in the final evaluation.

larger systems detection of fractional Chern insulators remains an open problem [45]. The challenge is rooted in the fact that topological order is by definition non-local and requires the evaluation of observables at extensively many sites simultaneously. While no conventional local order parameter exists in terms of the constituent particles, one can define a conventional order parameter for an effective model of composite particles including a flux attachment [46]. The fractional quantum Hall phase can be understood as a condensation of such composite bosons, signaled by an off-diagonal long-range order in the $g^{(1)}$ function of the composite particles.

A recent proposal discussed that this hidden order could be detected with cold atoms by measuring the phase coherence of one particle between two given sites i, j simultaneously with the positions $z_n = x_n + iy_n$ of all other particles, $n = 1, \dots, N - 1$. Combining the results in an appropriate correlator [46, 47] can then reveal the hidden order underlying the fractional quantum Hall effect. Specifically, the one-particle correlation function

for the composite bosons $\tilde{g}^{(1)}(\mathbf{i}, \mathbf{j})$, featuring long-range off-diagonal order in the fractional quantum Hall state, can be expressed in terms of the original annihilation (creation) operators in the form

$$\tilde{g}^{(1)}(\mathbf{i}, \mathbf{j}) = \left\langle \prod_{n=1}^{N-1} \left(\frac{z_{\mathbf{i}} - z_n}{|z_{\mathbf{i}} - z_n|} \right)^{-1/\nu} \left(\frac{z_{\mathbf{j}} - z_n}{|z_{\mathbf{j}} - z_n|} \right)^{1/\nu} \hat{a}_{\mathbf{i}}^\dagger \hat{a}_{\mathbf{j}} \right\rangle. \quad (7)$$

Here $z_{\mathbf{j}} = j_x + ij_y$ is the position in the complex plane corresponding to site \mathbf{j} , and ν is the filling factor, i.e., the number of particles per flux quantum. This expression shows that the composite boson correlation function picks up an additional non-trivial phase for each particle $n = 1 \dots N - 1$ not involving sites \mathbf{i}, \mathbf{j} with respect to the bare correlator $g^{(1)}(\mathbf{i}, \mathbf{j}) = \langle \hat{a}_{\mathbf{i}}^\dagger \hat{a}_{\mathbf{j}} \rangle$ and this correlation function can be accessed by combining a measurement of the coherence $g^{(1)}(\mathbf{i}, \mathbf{j})$ between sites \mathbf{i} and \mathbf{j} with a simultaneous measurement of the local occupations $\{\hat{n}_l\}_{l \neq \mathbf{i}, \mathbf{j}}$ at all other lattice sites.

The previous work suggested a realization of this hybrid measurement using a folded system, which allows connecting sites that are far apart [47]. Here we show that the matter-wave microscope allows accessing this nonlocal order without the need for difficult to realize geometries involving folding the system. The protocol is a variation of the protocol introduced in Fig. 1, but replaces the global final Raman pulse by a local pulse, which is focused onto a single lattice site via the microscope objective also used for imaging [48] (Fig. 4). Because the two different spin states at sites $\mathbf{l} \neq \mathbf{i}, \mathbf{j}$ are not coupled at the end of the sequence, they do not interfere and one can reconstruct the original density by summing the signal after moving back in space the shifted component during data evaluation. Adding a local $\pi/2$ Raman pulse at one site \mathbf{j} will lead to interference only there, allowing to combine the coherence between two sites with the density at all other sites as required for the correlator of Eq. (7). While measurements according to the protocol in Fig. 1 would access the phase coherence of the bare particles showing exponential decay, measurement according to Fig. 4 will access the phase coherence of the flux-attached composite bosons, showing algebraic decay. Based on the numerical study in [47], we expect that the measurement of the hidden off-diagonal long-range order requires only a few thousand snapshots.

The protocol discussed here mixes measurements of coherences and densities to reveal hidden order in fractional quantum Hall systems. Hidden order has also been revealed in 1D Mott insulators [4] and in the spin sector for 1D antiferromagnets with hole doping [6] and protocols similar to this one might identify so-far unknown hidden order parameters in Hubbard models, which may also include coherences.

VI. EXPERIMENTAL CONSIDERATIONS

We assume a realization with bosonic ^{133}Cs atoms for the protocols of Figs. 1 and 4 and with fermionic ^6Li atoms for the protocols of Figs. 2 and 3. The mass of the respective atom is m and we assume a lattice spacing of $a_{\text{lat}} = 500$ nm in both cases. For ^{133}Cs atoms, the Raman wavelength can be chosen around $\lambda = 870$ nm and we assume a first matter-wave lens with trap frequency $\omega_1 = 2\pi \times 50$ Hz, i.e., a pulse duration of 5 ms. The varying momentum transfer \mathbf{q} due to the Raman transition in Fourier plane will map to a displacement $\mathbf{d} = \hbar\mathbf{q}/(m\omega_1)$ in the image plane that is an integer multiple of the lattice spacing ($d = n \times a_{\text{lat}}$), in order to probe the coherence between lattice sites at varying distance.

For an angle θ between the Raman beams, the modulus of the momentum transfer is $q = (2\pi/\lambda)\sqrt{2(1 - \cos(\theta))}$ and a displacement over $n = 10$ lattice sites is achieved for an angle of $\theta = 30^\circ$ for ^{133}Cs atoms. The Raman beams can therefore enter through a state-of-the-art high-resolution objective (NA=0.5), which allows an easy change of the angle between the two beams [49]. For the ^6Li atoms, we assume a Raman wavelength at $\lambda = 671$ nm and a trap frequency of $\omega_1 = 2\pi \times 250$ Hz. In this case, a shift by $n = 10$ lattice sites can be realized via an angle between the Raman beams of only $\theta = 5^\circ$, which means that an angular precision around 0.05° is required for control to a fraction of a lattice site. In order to guarantee a stable phase reference, the Raman setup must be interferometrically stable and the beat signal between the two laser beams must be referenced to the start of the Raman pulse. For the second Raman pulse, when no momentum transfer is desired, the two laser beams should be co-propagating, but they can also be provided through the objective. The system remains confined in a 2D plane during the matter wave protocol in order to allow recapture in the lattice.

We assume throughout a matter-wave protocol with unit magnification, which only has the purpose to provide access to Fourier space. The atoms can then be reloaded into the original lattice at the end of the protocol, which can be used to freeze them for single-atom resolved imaging [1–3]. Spin-resolved single-atom imaging can be realized by splitting the two spin states along the perpendicular direction with suitable lattice manipulations [50], which will be insensitive to possible in-plane excitations from the recapture in the lattice. Alternatively, very large matter-wave magnifications can be combined with free-space fluorescence imaging [17]. A larger matter-wave magnification could help with the local Raman addressing in the image plane discussed in Fig. 4.

An important point for realizing the matter-wave microscope is to switch off interactions during the matter-wave protocol, because it relies on a single-particle picture. For the protocols using ^{133}Cs atoms, the physical spin is $F = 3$, $m_F = 3$ and the auxiliary spin is $F = 3$, $m_F = 2$. Due to the non-overlapping Feshbach resonances, the scattering lengths for the two states cannot

both be brought to zero, but one can quench the magnetic field to a point between the two zero-crossings [51]. To keep interaction effects low, we suggest to switch off the vertical confinement to rapidly decrease the density and add a matter-wave condition also in the vertical direction. In the protocols using ${}^6\text{Li}$ atoms, in contrast, a fast jump of the magnetic field from the much larger values is not feasible. Instead one can include rapid Raman spin flips into different spin states, which are weakly interacting at the given magnetic field [52], because the Feshbach resonances between different spin states are shifted relative to each other [53]. Furthermore, the magnetic field can be ramped to values close to zero during the matter-wave sequence in order to further reduce the interaction strength. The additional Raman pulses are applied at the beginning of the protocol together with a switch-off of the optical lattice in order to initiate the protocol. They are not included in Figs. 2 and 3 for clarity, but the extended protocol is discussed in Sec. IX D. These Raman pulses are realized with two co-propagating beams in order to avoid a momentum transfer. The duration of all Raman pulses in the protocols need to be short compared to the many-body time scales and compared to the duration of the matter-wave lenses in order to cause negligible displacement. With a trap frequency of $\omega_1 = 2\pi \times 250 \text{ Hz}$, i.e. quarter-period matter-wave lenses of $T = 1 \text{ ms}$ duration, and achievable Raman pulse durations down to 200 ns [52], this can be fulfilled.

In the protocol of Fig. 3, we select a momentum mode using a focused Raman beam in the Fourier space of the matter-wave microscope. We choose a suitable $1/e^2$ waist radius of the focused Raman beam w_0 and matter-wave trap frequency $\omega_1 = 2\pi \times 250 \text{ Hz}$ for the mapping from momentum space to real space $x = p/m\omega_1$. In order to select a mode width with typically one atom, we assume a system of 20 sites length and select a mode with of $1/20$ of the reciprocal lattice vector in momentum space, which corresponds to $w_0 = (h/a_{\text{lat}}/20)/(m\omega_1) = 4\mu\text{m}$ for ${}^6\text{Li}$ atoms. This can be tuned either via w_0 or ω_1 . For this waist size, the spread of wave vectors, which could cause a spread in the Raman momentum transfer, can be neglected.

The loading back into the lattice has to be realized as an inverse band mapping, which maps the isolated momentum mode onto a quasimomentum mode, i.e., an eigenstate of the lattice, which has no dispersion but only a trivial phase evolution of energy $\epsilon_{\mathbf{k}_0}$. In (inverse) band mapping, the time scale for ramping the lattice has to be slow compared to the single-particle band gaps, which can be around 100 μs for ${}^6\text{Li}$ atoms, which is fast compared to the matter-wave lens duration of $(2\pi/\omega_1)/4 = 1 \text{ ms}$.

We assume that the original system has a very weak overall confinement or a box potential and that the confinement with trap frequency ω_1 is switched on rapidly for the matter-wave lenses only. It is then not a limitation for the (inverse) band mapping time scale. With an angle of 30° between the Raman lasers, the isolated mode is

shifted by $n_{\text{iso}} = 68$ lattice sites. For the many-body evolution, it can then be loaded into an isolated region of the lattice of this size, possibly bounded by an additional box potential. Because the quasi momentum mode is not an exact eigenstate of a finite system, we expect a dephasing with a frequency around J/n_{iso} with the tunneling energy J , which sets one (tolerable) limitation on the achievable frequency resolution. Loading back into the lattice also requires excellent phase stability of the lattice over the duration of the matter-wave protocol and a high-fidelity matter-wave imaging of the original distribution without aberration-induced shifts. Reloading with good matching of the wave function to the lattice was demonstrated after time evolutions on the order of a Talbot time in [54]. Note that in the case of a lattice with inversion-symmetry breaking such as a superlattice, one should use a $3T/4$ matter wave lens in order to avoid the inverting imaging of the $T/4$ pulse.

VII. CONCLUSION AND OUTLOOK

Our results show the great potential of matter-wave microscopy for accessing exotic correlators including phases and coherences and for characterizing intriguing quantum many-body states. We expect that more protocols for relevant correlators can be found. E.g. extensions of the scheme for non-equal time correlators to negative time evolutions from inverting the sign of every term in the Hamiltonian [55] might also give access to out-of-time-order correlators, which provide a proxy for diagnosing chaos in quantum systems such as for distinguishing ergodic from non-ergodic dynamics in the context of many-body localization [56, 57]. Furthermore, phase coherence is an interesting signature for Majorana zero modes at the edges of a 1D topological system, where the two-point correlation function $\langle \hat{a}_1^\dagger \hat{a}_j \rangle$ exponentially decays in the bulk and has a revival at the other end of the chain [58]. Similarly, power-law decay of $g^{(1)}$ correlations along edges of fractional quantum Hall states can be probed. It might also be worthwhile to study which further information the correlators discussed here can provide similar to the extraction of transport coefficients from many current measurements as proposed in [59]. Moreover, the scheme could be extended to continuous (non-lattice) systems. Finally, going beyond the four-point correlators discussed for the superconducting order, the interference of many-body systems might be useful to extract other relevant quantities such as entanglement entropy as realized in many-body Hong-Ou Mandel starting from two copies of the system [60].

VIII. ACKNOWLEDGMENTS

C.W. acknowledges support by the Deutsche Forschungsgemeinschaft (DFG, German Research Foundation) via the Research Unit FOR 5688 (Project

No. 521530974). O.C. and F.G. received funding from the European Research Council (ERC) under the European Union's Horizon 2020 research and innovation programme (Grant Agreement no 948141) — ERC Starting Grant SimUcQuam. A.B. received funding from the European Research Council (ERC) under the European Union's Horizon 2020 research and innovation programme (Grant Agreement No. 101217531) — ERC Starting Grant QuaQuaMA. O.C., A.B. and F.G. acknowledge funding by the Deutsche Forschungsgemeinschaft (DFG, German Research Foundation) under Germany's Excellence Strategy – EXC-2111 – 390814868.

IX. APPENDIX

A. Heisenberg picture gates

The precise quantities measured after manipulation by matter-wave lenses and Raman beams can be understood by the corresponding evolution of operators in the Heisenberg picture, where both lenses and pulses can be modeled as single-particle gates. From knowing how arbitrary states transform, we can write down conjugation with the associated time evolution operators \mathcal{U}_{MaW} (Matter-wave lenses) and \mathcal{U}_{R} (Raman pulses):

$$\begin{aligned}\mathcal{U}_{\text{MaW}} \hat{a}_{\mathbf{x}\uparrow/\downarrow}^\dagger \mathcal{U}_{\text{MaW}}^\dagger &= \hat{a}_{-\mathbf{k}\uparrow/\downarrow}^\dagger \\ \mathcal{U}_{\text{MaW}} \hat{a}_{\mathbf{k}\uparrow/\downarrow}^\dagger \mathcal{U}_{\text{MaW}}^\dagger &= \hat{a}_{\mathbf{x}\uparrow/\downarrow}^\dagger \\ \mathcal{U}_{\text{R}} \begin{pmatrix} \hat{a}_{\mathbf{k}\uparrow}^\dagger \\ \hat{a}_{\mathbf{k}+\mathbf{q}\downarrow}^\dagger \end{pmatrix} \mathcal{U}_{\text{R}}^\dagger &= \frac{1}{\sqrt{2}} \begin{pmatrix} 1 & e^{i\varphi} \\ -e^{-i\varphi} & 1 \end{pmatrix} \begin{pmatrix} \hat{a}_{\mathbf{k}\uparrow}^\dagger \\ \hat{a}_{\mathbf{k}+\mathbf{q}\downarrow}^\dagger \end{pmatrix} \\ \mathcal{U}_{\text{R},\mathbf{q}=0} \begin{pmatrix} \hat{a}_{\mathbf{x}\uparrow}^\dagger \\ \hat{a}_{\mathbf{x}\downarrow}^\dagger \end{pmatrix} \mathcal{U}_{\text{R},\mathbf{q}=0}^\dagger &= \frac{1}{\sqrt{2}} \begin{pmatrix} 1 & e^{i\varphi} \\ -e^{-i\varphi} & 1 \end{pmatrix} \begin{pmatrix} \hat{a}_{\mathbf{x}\uparrow}^\dagger \\ \hat{a}_{\mathbf{x}\downarrow}^\dagger \end{pmatrix}.\end{aligned}$$

The time evolutions of operators in the Heisenberg picture are the inverses of this, i.e. we make use of

$$\begin{aligned}\mathcal{U}_{\text{MaW}}^\dagger \hat{a}_{\mathbf{k}\uparrow/\downarrow}^\dagger \mathcal{U}_{\text{MaW}} &= \hat{a}_{-\mathbf{x}\uparrow/\downarrow}^\dagger \\ \mathcal{U}_{\text{MaW}}^\dagger \hat{a}_{\mathbf{x}\uparrow/\downarrow}^\dagger \mathcal{U}_{\text{MaW}} &= \hat{a}_{\mathbf{k}\uparrow/\downarrow}^\dagger \\ \mathcal{U}_{\text{R}}^\dagger \begin{pmatrix} \hat{a}_{\mathbf{k}\uparrow}^\dagger \\ \hat{a}_{\mathbf{k}+\mathbf{q}\downarrow}^\dagger \end{pmatrix} \mathcal{U}_{\text{R}} &= \frac{1}{\sqrt{2}} \begin{pmatrix} 1 & -e^{i\varphi} \\ e^{-i\varphi} & 1 \end{pmatrix} \begin{pmatrix} \hat{a}_{\mathbf{k}\uparrow}^\dagger \\ \hat{a}_{\mathbf{k}+\mathbf{q}\downarrow}^\dagger \end{pmatrix} \\ \mathcal{U}_{\text{R},\mathbf{q}=0}^\dagger \begin{pmatrix} \hat{a}_{\mathbf{x}\uparrow}^\dagger \\ \hat{a}_{\mathbf{x}\downarrow}^\dagger \end{pmatrix} \mathcal{U}_{\text{R},\mathbf{q}=0} &= \frac{1}{\sqrt{2}} \begin{pmatrix} 1 & -e^{i\varphi} \\ e^{-i\varphi} & 1 \end{pmatrix} \begin{pmatrix} \hat{a}_{\mathbf{x}\uparrow}^\dagger \\ \hat{a}_{\mathbf{x}\downarrow}^\dagger \end{pmatrix}.\end{aligned}$$

These gates can then be applied to relate operators between the interferometer steps:

$$\hat{a}^\dagger(n) = \mathcal{U}_n^\dagger \hat{a}^\dagger(n-1) \mathcal{U}_n,$$

where $\hat{a}^\dagger(n)$ denotes any creation operator after sequence step n . The initial operators, encoding observables of the initial state, are written without parentheses.

For example, following the scheme of Fig. 1, applying the initial matter-wave lens maps

$$\hat{a}_{\mathbf{k},\uparrow/\downarrow}^\dagger(1) = \hat{a}_{-\mathbf{x},\uparrow/\downarrow}^\dagger.$$

Here steps are enumerated as in Fig. 1. The Raman pulse of momentum transfer \mathbf{q} gives the Heisenberg operators after the second step

$$\begin{pmatrix} \hat{a}_{\mathbf{x},\uparrow}^\dagger(2) \\ \hat{a}_{\mathbf{k}+\mathbf{q},\downarrow}^\dagger(2) \end{pmatrix} = \frac{1}{\sqrt{2}} \begin{pmatrix} 1 & -1 \\ 1 & 1 \end{pmatrix} \begin{pmatrix} \hat{a}_{-\mathbf{x}\uparrow}^\dagger \\ \hat{a}_{-\mathbf{x}-\mathbf{d}\downarrow}^\dagger \end{pmatrix},$$

where \mathbf{d} is the real-space kick corresponding to \mathbf{q} , etc.

The composition yields the operators after all interferometer steps in terms of the initial operators:

$$\begin{pmatrix} \hat{a}_{\mathbf{x},\uparrow}^\dagger(4) \\ \hat{a}_{\mathbf{x},\downarrow}^\dagger(4) \end{pmatrix} = \frac{1}{2} \begin{pmatrix} \hat{a}_{-\mathbf{x},\uparrow}^\dagger - e^{i\varphi} \hat{a}_{-\mathbf{x}+\mathbf{d},\uparrow}^\dagger - \hat{a}_{-\mathbf{x}-\mathbf{d},\downarrow}^\dagger - e^{i\varphi} \hat{a}_{-\mathbf{x},\downarrow}^\dagger \\ e^{-i\varphi} \hat{a}_{-\mathbf{x},\uparrow}^\dagger + \hat{a}_{-\mathbf{x}+\mathbf{d},\uparrow}^\dagger - e^{-i\varphi} \hat{a}_{-\mathbf{x}-\mathbf{d},\downarrow}^\dagger + \hat{a}_{-\mathbf{x},\downarrow}^\dagger \end{pmatrix}.$$

For a system invariant under time-reversal (complex conjugation), $g^{(1)} = \langle \hat{a}_{\mathbf{x}+\mathbf{d},\uparrow}^\dagger \hat{a}_{\mathbf{x},\uparrow} \rangle = \langle \hat{a}_{\mathbf{x}+\mathbf{d},\uparrow}^\dagger \hat{a}_{\mathbf{x},\uparrow} \rangle^* = g^{(1)*}$ implies that two-point correlators offdiagonal in space are real. Evaluating the density expectation value for a spin-polarized state then yields Equation (4).

B. *d*-wave superconducting order

For the interferometer described in Fig. 2, each physical spin leg is coupled through the Raman pulses to an auxiliary spin $\uparrow\sim\uparrow\uparrow, \downarrow\sim\downarrow\downarrow$. The Raman momentum kicks $\mathbf{d}_1, \mathbf{d}_2$, and phases φ_1, φ_2 , are also kept separate, such that the result reads

$$\begin{aligned}\begin{pmatrix} \hat{a}_{\mathbf{x}_1,\uparrow}^\dagger(4) \\ \hat{a}_{\mathbf{x}_1,\uparrow}^\dagger(4) \end{pmatrix} &= \frac{1}{2} \begin{pmatrix} \hat{a}_{-\mathbf{x}_1,\uparrow}^\dagger - e^{i\varphi_1} \hat{a}_{-\mathbf{x}_1+\mathbf{d}_1,\uparrow}^\dagger - \hat{a}_{-\mathbf{x}_1-\mathbf{d}_1,\uparrow}^\dagger - e^{i\varphi_1} \hat{a}_{-\mathbf{x}_1,\uparrow}^\dagger \\ e^{-i\varphi_1} \hat{a}_{-\mathbf{x}_1,\uparrow}^\dagger + \hat{a}_{-\mathbf{x}_1+\mathbf{d}_1,\uparrow}^\dagger - e^{-i\varphi_1} \hat{a}_{-\mathbf{x}_1-\mathbf{d}_1,\uparrow}^\dagger + \hat{a}_{-\mathbf{x}_1,\uparrow}^\dagger \end{pmatrix}, \\ \begin{pmatrix} \hat{a}_{\mathbf{x}_2,\downarrow}^\dagger(4) \\ \hat{a}_{\mathbf{x}_2,\downarrow}^\dagger(4) \end{pmatrix} &= \frac{1}{2} \begin{pmatrix} \hat{a}_{-\mathbf{x}_2,\downarrow}^\dagger - e^{i\varphi_2} \hat{a}_{-\mathbf{x}_2+\mathbf{d}_2,\downarrow}^\dagger - \hat{a}_{-\mathbf{x}_2-\mathbf{d}_2,\downarrow}^\dagger - e^{i\varphi_2} \hat{a}_{-\mathbf{x}_2,\downarrow}^\dagger \\ e^{-i\varphi_2} \hat{a}_{-\mathbf{x}_2,\downarrow}^\dagger + \hat{a}_{-\mathbf{x}_2+\mathbf{d}_2,\downarrow}^\dagger - e^{-i\varphi_2} \hat{a}_{-\mathbf{x}_2-\mathbf{d}_2,\downarrow}^\dagger + \hat{a}_{-\mathbf{x}_2,\downarrow}^\dagger \end{pmatrix}.\end{aligned}$$

Taking the initial state to be spin polarized then drops all reference to the auxiliary spins. We find the target correlator in Equation (5) when selecting e.g. $\mathbf{x}_1 = -\mathbf{j}$, $\mathbf{d}_1 = \mathbf{i} - \mathbf{j}$, $\mathbf{x}_2 = -\mathbf{j} - \mathbf{e}_\nu$, $\mathbf{d}_2 = \mathbf{i} - \mathbf{j} + \mathbf{e}_\mu - \mathbf{e}_\nu$, such that density measurements read

$$\begin{aligned}
\langle \hat{n}_{-\mathbf{j}\uparrow}(4) \hat{n}_{-\mathbf{j}-\mathbf{e}_y \nu\downarrow}(4) \rangle &= \frac{1}{2^4} \langle (\hat{n}_{\mathbf{j}\uparrow} + \hat{n}_{\mathbf{i}\uparrow})(\hat{n}_{\mathbf{j}+\mathbf{e}_\nu\downarrow} + \hat{n}_{\mathbf{i}+\mathbf{e}_\mu\downarrow}) + (\hat{n}_{\mathbf{j}\uparrow} + \hat{n}_{\mathbf{i}\uparrow})(-e^{i\varphi_2} \hat{a}_{\mathbf{i}+\mathbf{e}_\mu\downarrow}^\dagger \hat{a}_{\mathbf{j}+\mathbf{e}_\nu\downarrow} + \text{h.c.}) \\
&\quad + (-e^{i\varphi_1} \hat{a}_{\mathbf{i}\uparrow}^\dagger \hat{a}_{\mathbf{j}\uparrow} + \text{h.c.})(\hat{n}_{\mathbf{j}+\mathbf{e}_\nu\downarrow} + \hat{n}_{\mathbf{i}+\mathbf{e}_\mu\downarrow}) - I \rangle \\
I &= (e^{i\varphi_1} \hat{a}_{\mathbf{i}\uparrow}^\dagger \hat{a}_{\mathbf{j}\uparrow} + \text{h.c.})(e^{i\varphi_2} \hat{a}_{\mathbf{i}+\mathbf{e}_\mu\downarrow}^\dagger \hat{a}_{\mathbf{j}+\mathbf{e}_\nu\downarrow} + \text{h.c.}) \\
&= e^{i(\varphi_1+\varphi_2)} \hat{a}_{\mathbf{i}\uparrow}^\dagger \hat{a}_{\mathbf{j}\uparrow} \hat{a}_{\mathbf{i}+\mathbf{e}_\mu\downarrow}^\dagger \hat{a}_{\mathbf{j}+\mathbf{e}_\nu\downarrow} + e^{i(\varphi_1-\varphi_2)} \hat{a}_{\mathbf{i}\uparrow}^\dagger \hat{a}_{\mathbf{j}\uparrow} \hat{a}_{\mathbf{j}+\mathbf{e}_\nu\downarrow}^\dagger \hat{a}_{\mathbf{i}+\mathbf{e}_\mu\downarrow} + \text{h.c.}
\end{aligned} \tag{8}$$

The evaluation can be greatly simplified by that the desired four-point correlator is expected to be real. Furthermore, the cross-terms of the form $(\hat{n}_{\mathbf{j}\uparrow} + \hat{n}_{\mathbf{i}\uparrow})(-e^{-i\varphi_2} \hat{a}_{\mathbf{i}+\mathbf{e}_\mu\downarrow}^\dagger \hat{a}_{\mathbf{j}+\mathbf{e}_\nu\downarrow} + \text{h.c.})$ are real for time reversal symmetric systems, and the desired correlator can be directly obtained from the combination of four measurements with different Raman phases $\varphi_1 = \varphi_2 = \varphi$.

$$\begin{aligned}
\langle \hat{n}_{-\mathbf{j}}(4) \hat{n}_{-\mathbf{j}-\mathbf{e}_\nu}(4) \rangle_{\varphi=0} &+ \langle \hat{n}_{-\mathbf{j}}(4) \hat{n}_{-\mathbf{j}-\mathbf{e}_\nu}(4) \rangle_{\varphi=\pi} \\
- \langle \hat{n}_{-\mathbf{j}}(4) \hat{n}_{-\mathbf{j}-\mathbf{e}_\nu}(4) \rangle_{\varphi=\pi/2} &- \langle \hat{n}_{-\mathbf{j}}(4) \hat{n}_{-\mathbf{j}-\mathbf{e}_\nu}(4) \rangle_{\varphi=-\pi/2} \\
= \frac{1}{2} \langle \hat{a}_{\mathbf{i}\uparrow}^\dagger \hat{a}_{\mathbf{i}+\mathbf{e}_\mu\downarrow}^\dagger \hat{a}_{\mathbf{j}\uparrow} \hat{a}_{\mathbf{j}+\mathbf{e}_\nu\downarrow} \rangle &= \frac{1}{2} C_{\mu,\nu}(\mathbf{i} - \mathbf{j}). \tag{9}
\end{aligned}$$

This can be seen as follows. The first term in Eq. (8) is independent of Raman phases, so the two positive and two negative measurements in Eq. (9) cancel these contributions. The second and third terms contain go as $\cos(\varphi_1)$ and $\cos(\varphi_2)$, so the measurements with Raman phases $\varphi_1 = \varphi_2 = 0$ and π cancel these out, while they are zero for the measurements with $\varphi_1 = \varphi_2 = \pi/2$ and $-\pi/2$. Finally the second term of I cancels out between the measurements with Raman phases $\varphi_1 = \varphi_2 = \pm\pi/2$ and $\pi, 0$, while the first term of I adds up, between the same pairs of chosen phases, to the desired correlator. As we consider fermions for this protocol, anticommutation of the different spin sectors has here been used in the final step.

C. Non-equal time correlations and ARPES spectra

For the out-of-time correlation functions we consider the following sequence of gates:

1. MaW lens $\begin{pmatrix} \hat{a}_{\mathbf{k}\uparrow/\downarrow}^\dagger(1) \\ \hat{a}_{\mathbf{x}\uparrow/\downarrow}^\dagger(1) \end{pmatrix} = \begin{pmatrix} \hat{a}_{-\mathbf{x}\uparrow/\downarrow}^\dagger \\ \hat{a}_{\mathbf{k}\uparrow/\downarrow}^\dagger \end{pmatrix}$
2. Local Raman $\begin{pmatrix} \hat{a}_{\mathbf{x}\uparrow}^\dagger(2) \\ \hat{a}_{\mathbf{x}\downarrow}^\dagger(2) \end{pmatrix} = \frac{g(\mathbf{x} - \mathbf{x}_0)}{\sqrt{2}} \begin{pmatrix} 1 & -e^{i\mathbf{q}\mathbf{x}} \\ e^{-i\mathbf{q}\mathbf{x}} & 1 \end{pmatrix} \begin{pmatrix} \hat{a}_{\mathbf{x}\uparrow}^\dagger(1) \\ \hat{a}_{\mathbf{x}\downarrow}^\dagger(1) \end{pmatrix} + \frac{\sqrt{2 - g(\mathbf{x} - \mathbf{x}_0)^2} - g(\mathbf{x} - \mathbf{x}_0)}{\sqrt{2}} \mathbb{I} \begin{pmatrix} \hat{a}_{\mathbf{x}\uparrow}^\dagger(1) \\ \hat{a}_{\mathbf{x}\downarrow}^\dagger(1) \end{pmatrix}$
3. MaW lens $\begin{pmatrix} \hat{a}_{\mathbf{k}\uparrow/\downarrow}^\dagger(3) \\ \hat{a}_{\mathbf{x}\uparrow/\downarrow}^\dagger(3) \end{pmatrix} = \begin{pmatrix} \hat{a}_{-\mathbf{x}\uparrow/\downarrow}^\dagger(2) \\ \hat{a}_{\mathbf{k}\uparrow/\downarrow}^\dagger(2) \end{pmatrix}$

4. Time evolution

$$\begin{cases} \hat{a}_{\mathbf{x}\uparrow/\downarrow}^\dagger(4) = \mathfrak{U}(t) \hat{a}_{\mathbf{x}\uparrow/\downarrow}^\dagger(3), & |\mathbf{x}| < |\frac{d}{2}| \\ \hat{a}_{\mathbf{x}\uparrow/\downarrow}^\dagger(4) = e^{i\hat{H}_0 t} \hat{a}_{\mathbf{x}\uparrow/\downarrow}^\dagger(3) e^{-i\hat{H}_0 t}, & |\mathbf{x}| > |\frac{d}{2}| \end{cases}$$

$$5. \text{ MaW lens } \begin{pmatrix} \hat{a}_{\mathbf{k}\uparrow/\downarrow}^\dagger(5) \\ \hat{a}_{\mathbf{x}\uparrow/\downarrow}^\dagger(5) \end{pmatrix} = \begin{pmatrix} \hat{a}_{-\mathbf{x}\uparrow/\downarrow}^\dagger(4) \\ \hat{a}_{\mathbf{k}\uparrow/\downarrow}^\dagger(4) \end{pmatrix}$$

6. Local Raman

$$\begin{pmatrix} \hat{a}_{-\mathbf{x}\uparrow}^\dagger(6) \\ \hat{a}_{-\mathbf{x}\downarrow}^\dagger(6) \end{pmatrix} = \frac{g(\mathbf{x} - \mathbf{x}_0)}{\sqrt{2}} \begin{pmatrix} 1 & -e^{i\varphi + i\mathbf{q}\mathbf{x}} \\ e^{-i\varphi - i\mathbf{q}\mathbf{x}} & 1 \end{pmatrix} \begin{pmatrix} \hat{a}_{-\mathbf{x}\uparrow}^\dagger(5) \\ \hat{a}_{-\mathbf{x}\downarrow}^\dagger(5) \end{pmatrix} + \frac{\sqrt{2 - g(\mathbf{x} - \mathbf{x}_0)^2} - g(\mathbf{x} - \mathbf{x}_0)}{\sqrt{2}} \mathbb{I} \begin{pmatrix} \hat{a}_{-\mathbf{x}\uparrow}^\dagger(5) \\ \hat{a}_{-\mathbf{x}\downarrow}^\dagger(5) \end{pmatrix}$$

The last Raman pulse could alternatively be applied globally, because the interference is only evaluated locally. Here the momentum kicks of the Raman beams have been incorporated through the phase factors $e^{i\mathbf{q}\mathbf{x}}$ allowing a complete real-space representation, and the targeting of a specific mode is carried out by the envelope $g(\mathbf{x} - \mathbf{x}_0, w_0/2)$ which falls off at a length scale $w_0/2$, normalized to a value of one at $\mathbf{x} = \mathbf{x}_0$ (w_0 omitted in many formulae for clarity). The precise shape of this envelope is not crucial to the following argument, but we take it to be of gaussian form $g(\mathbf{x}, w_0/2) = e^{-2|\mathbf{x}|^2/w_0^2}$, such that $w_0/2$ is the standard deviation of the envelope. Note how the Raman gates are complemented by additional diagonal terms away from $\mathbf{x} = \mathbf{x}_0$ to ensure unitarity. Contributions due to these drop when measuring at $-\mathbf{x}_0$.

The time evolution of step (4) follows the fully interacting Hamiltonian \hat{H} , encoded in the superoperator $\mathfrak{U}(t) \hat{a}_k^\dagger = e^{i\hat{H}t} \hat{a}_k^\dagger e^{-i\hat{H}t}$, for operators with support on the initial extent of the system, here assumed to be $|\mathbf{x}| < |\frac{d}{2}|$. Since only a small fraction of the system is removed from this region by the Raman beam (2), the outside of this initial extent $|\mathbf{x}| > |\frac{d}{2}|$ is sufficiently dilute for the dynamics to rather be ruled by a non-interacting Hamiltonian \hat{H}_0 . This split in the time evolution can be conveniently incorporated by noting that contributions to $\hat{a}_{\mathbf{x}\uparrow/\downarrow}(4) \sim \int d\mathbf{k}' e^{i\mathbf{k}'\cdot\mathbf{x}} f_{\mathbf{k}'}$, where $f_{\mathbf{k}} = g(\mathbf{x} - \mathbf{x}_0, w_0/2) e^{i\mathbf{q}\mathbf{x}} \hat{a}_{\mathbf{k}\uparrow/\downarrow}^\dagger$, only have support on the isolated region $|\mathbf{x}| > |\frac{d}{2}|$ when w_0 is sufficiently broad

with respect to the momentum kick \mathbf{q} . This follows from

$$\begin{aligned} & \int d\mathbf{k}' e^{i\mathbf{k}' \cdot \mathbf{x}} g(\mathbf{x}' - \mathbf{x}_0, w_0/2) e^{\mathbf{q} \cdot \mathbf{x}'} \hat{a}_{\mathbf{k}' \uparrow/\downarrow}^\dagger \\ &= \int d\mathbf{k}' e^{i\mathbf{k}' \cdot \mathbf{x}} g((\mathbf{k}' - \mathbf{k}_0), \frac{m\omega_1}{2\hbar} w_0) e^{i\mathbf{k}' \cdot \mathbf{d}} \hat{a}_{\mathbf{k}' \uparrow/\downarrow}^\dagger \\ &= (\tilde{g}(\mathbf{x}, \frac{2\hbar}{m\omega_1} w_0^{-1}) e^{i\mathbf{k}_0 \cdot \mathbf{x}}) * \hat{a}_{\mathbf{x} + \mathbf{d} \uparrow/\downarrow}^\dagger. \end{aligned}$$

Here \tilde{g} denotes the Fourier transform of g , with corresponding inversion of the characteristic width. E.g. for g gaussian, this is another gaussian $\tilde{g}(\mathbf{x}, w_0^{-1}/2) \sim e^{-2|\mathbf{x}|^2/w_0^{-2}}$. The convolution $(*)$ then ensures that only operators acting a distance $\frac{2\hbar}{m\omega_1} w_0^{-1}$ away from $\mathbf{x} + \mathbf{d}$

take part in this object. With the width w_0 corresponding to the e^{-2} waist radius 4 μm suggested in Sec. VI, and with the momentum kick $\mathbf{q} = \frac{m\omega_1}{\hbar} \mathbf{d}$ on the order of the Raman wavenumber $2\pi\lambda^{-1} = 2\pi/671 \text{ nm}^{-1}$, we find that the relative spread of f with respect to \mathbf{d} is a few percent percent, $\lambda/(\pi w_0) = 0.05$. The support of terms arising from $f_{\mathbf{k}}$ is then completely delocalized from the initial system location, and for step (4) such terms take on trivial time evolution $\hat{a}_{\mathbf{k} \uparrow/\downarrow}^\dagger(4) = e^{i\varepsilon_{\mathbf{k}} t} \hat{a}_{\mathbf{k} \uparrow/\downarrow}^\dagger(3)$, where $\varepsilon_{\mathbf{k}}$ is the dispersion of the non-interacting lattice system. Remaining terms have support on the initial system location, and follow the interacting time evolution.

With this preliminary in hand, we turn to composing the gates. With $h(\mathbf{x} - \mathbf{x}_0) = \sqrt{2 - g(\mathbf{x} - \mathbf{x}_0)^2}$ the magnitude of the diagonals of the Raman gates, we find that:

$$\begin{aligned} \begin{pmatrix} \hat{a}_{-\mathbf{k}\uparrow}^\dagger(4) \\ \hat{a}_{-\mathbf{k}\downarrow}^\dagger(4) \end{pmatrix} &= \frac{1}{\sqrt{2}} \begin{pmatrix} h(\mathbf{x} - \mathbf{x}_0) \mathfrak{U}(t) & -g(\mathbf{x} - \mathbf{x}_0) e^{i\mathbf{q} \cdot \mathbf{x} + i\varepsilon_{\mathbf{k}} t} \\ g(\mathbf{x} - \mathbf{x}_0) e^{-i\mathbf{q} \cdot \mathbf{x} + i\varepsilon_{\mathbf{k}} t} & h(\mathbf{x} - \mathbf{x}_0) \mathfrak{U}(t) \end{pmatrix} \begin{pmatrix} \hat{a}_{\mathbf{k}\uparrow}^\dagger \\ \hat{a}_{\mathbf{k}\downarrow}^\dagger \end{pmatrix} \\ \begin{pmatrix} \hat{a}_{-\mathbf{x}\uparrow}^\dagger(6) \\ \hat{a}_{-\mathbf{x}\downarrow}^\dagger(6) \end{pmatrix} &= \frac{1}{\sqrt{2}} \begin{pmatrix} h(\mathbf{x} - \mathbf{x}_0) & -g(\mathbf{x} - \mathbf{x}_0) e^{i\varphi + i\mathbf{q} \cdot \mathbf{x}} \\ g(\mathbf{x} - \mathbf{x}_0) e^{-i\varphi - i\mathbf{q} \cdot \mathbf{x}} & h(\mathbf{x} - \mathbf{x}_0) \end{pmatrix} \begin{pmatrix} \hat{a}_{-\mathbf{k}\uparrow}^\dagger(4) \\ \hat{a}_{-\mathbf{k}\downarrow}^\dagger(4) \end{pmatrix} \\ &= \frac{1}{2} \begin{pmatrix} h(\mathbf{x} - \mathbf{x}_0)^2 \mathfrak{U}(t) - g(\mathbf{x} - \mathbf{x}_0)^2 e^{i\varphi + i\varepsilon_{\mathbf{k}} t} & -g(\mathbf{x} - \mathbf{x}_0) h(\mathbf{x} - \mathbf{x}_0) (e^{i\mathbf{q} \cdot \mathbf{x} + i\varepsilon_{\mathbf{k}} t} + \mathfrak{U}(t) e^{i\varphi + i\mathbf{q} \cdot \mathbf{x}}) \\ g(\mathbf{x} - \mathbf{x}_0) h(\mathbf{x} - \mathbf{x}_0) (\mathfrak{U}(t) e^{-i\varphi - i\mathbf{q} \cdot \mathbf{x}} + e^{i\varepsilon_{\mathbf{k}} t - i\mathbf{q} \cdot \mathbf{x}}) & h(\mathbf{x} - \mathbf{x}_0)^2 \mathfrak{U}(t) - g(\mathbf{x} - \mathbf{x}_0)^2 e^{-i\varphi + i\varepsilon_{\mathbf{k}} t} \end{pmatrix} \begin{pmatrix} \hat{a}_{\mathbf{k}\uparrow}^\dagger \\ \hat{a}_{\mathbf{k}\downarrow}^\dagger \end{pmatrix}. \end{aligned}$$

The offdiagonal terms drop out as explained above. When measuring at the focus of the Raman beam the Gaussian envelope also no longer plays any role and we find, with $\hat{a}(t)$ denoting annihilation operators time-evolved under the interacting Hamiltonian, a fringe proportional to $G(\mathbf{k}_0, t) = -i\Theta(t)\langle \hat{a}_{\mathbf{k}_0\uparrow}^\dagger(t)\hat{a}_{\mathbf{k}_0\uparrow}(0) \rangle$:

$$\langle \hat{n}_{-\mathbf{x}_0\uparrow}(6) \rangle = \frac{1}{4} (\langle \hat{n}_{\mathbf{k}_0\uparrow} \rangle - e^{-i\varphi - i\varepsilon_{\mathbf{k}_0} t} \langle \hat{a}_{\mathbf{k}_0\uparrow}^\dagger(t)\hat{a}_{\mathbf{k}_0\uparrow}(0) \rangle + \text{h.c.}).$$

D. Extended protocol for controlling interactions

For controlling the interactions in a spinful system, which propose to make a spin flip (a Raman π pulse) between strongly interacting physical spin states and weakly-interacting auxiliary spin states. Fig. 5 shows how the protocol of 3 is modified by adding the required spin flips.

- [1] W. S. Bakr, A. Peng, M. E. Tai, R. Ma, J. Simon, J. I. Gillen, S. Fölling, L. Pollet, and M. Greiner, *Science* **329**, 547 (2010).
- [2] J. F. Sherson, C. Weitenberg, M. Endres, M. Cheneau, I. Bloch, and S. Kuhr, *Nature* **467**, 68–72 (2010).
- [3] C. Gross and W. S. Bakr, *Nature Physics* **17**, 1316 (2021).
- [4] M. Endres, M. Cheneau, T. Fukuhara, C. Weitenberg, P. Schauß, C. Gross, L. Mazza, M. C. Bañuls, L. Pollet, I. Bloch, and S. Kuhr, *Science* **334**, 200 (2011), <https://www.science.org/doi/pdf/10.1126/science.1209284>.
- [5] J. Koepsell, J. Vijayan, P. Sompé, F. Grusdt, T. A. Hilker, E. Demler, G. Salomon, I. Bloch, and C. Gross, *Nature* **572**, 358 (2019).
- [6] T. A. Hilker, G. Salomon, F. Grusdt, A. Omran, M. Boll, E. Demler, I. Bloch, and C. Gross, *Science* **357**, 484 (2017), <https://www.science.org/doi/pdf/10.1126/science.aam8990>.
- [7] M. Killi, S. Trotzky, and A. Paramekanti, *Phys. Rev. A* **86**, 063632 (2012).
- [8] M. Knap, A. Kantian, T. Giamarchi, I. Bloch, M. D. Lukin, and E. Demler, *Phys. Rev. Lett.* **111**, 147205 (2013).
- [9] S. Kehl and F. Marquardt, *Phys. Rev. A* **89**, 061601 (2014).
- [10] A. Kosior and K. Sacha, *Phys. Rev. Lett.* **112**, 045302 (2014).
- [11] L. A. Peña Ardila, M. Heyl, and A. Eckardt, *Phys. Rev. Lett.* **121**, 260401 (2018).
- [12] P. A. Murthy and S. Jochim, (2019), arXiv:1911.10824 [cond-mat.quant-gas].
- [13] A. Impertro, S. Karch, J. F. Wienand, S. Huh, C. Schweizer, I. Bloch, and M. Aidelsburger, *Phys. Rev. Lett.* **133**, 063401 (2024).

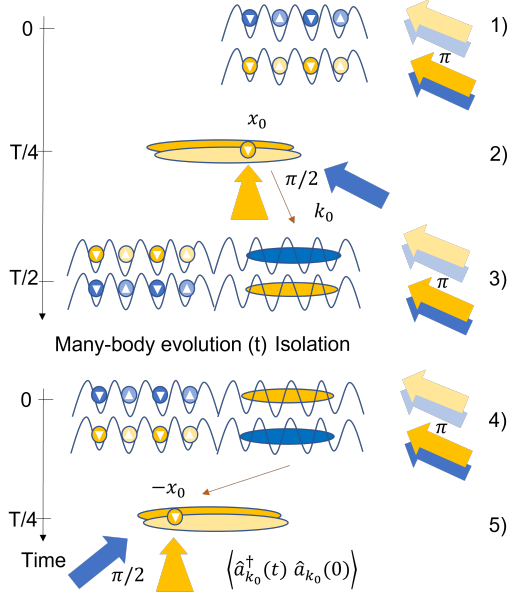


FIG. 5. Protocol of Fig. 3 but for a spinful initial system, realized with ${}^6\text{Li}$ atoms. Appropriate spin flips ensure weak interactions during the matter-wave protocol, but strong interactions in the initial system and during the time evolution of the recaptured system with one momentum mode isolated. Immediately after switching off the lattice, a Raman transfer (π pulse) without momentum kick into the upper hyperfine states is applied and reduces the interaction strength during the matter-wave protocol. The same idea can be used in the protocol of Fig. 2 and combined with a ramp down of the magnetic field after the first π pulse.

- [14] A. Impertro, S. Huh, S. Karch, J. F. Wienand, I. Bloch, and M. Aidelsburger, *Nature Physics* **21**, 895 (2025).
- [15] J. C. Brüggenjürgen, M. S. Fischer, and C. Weitenberg, A phase microscope for quantum gases (2024), arXiv:2410.10611 [cond-mat.quant-gas].
- [16] L. Asteria, H. P. Zahn, M. N. Kosch, K. Sengstock, and C. Weitenberg, *Nature* **599**, 571 (2021).
- [17] S. Brandstetter, C. Heintze, P. Hill, P. M. Preiss, M. Gałka, and S. Jochim, *Phys. Rev. Lett.* **135**, 103401 (2025).
- [18] L. Asteria, PhD thesis, Universität Hamburg (2022).
- [19] C. Roth, A. Chen, A. Sengupta, and A. Georges, Superconductivity in the two-dimensional hubbard model revealed by neural quantum states (2025), arXiv:2511.07566 [cond-mat.supr-con].
- [20] M. Xu, L. H. Kendrick, A. Kale, Y. Gang, C. Feng, S. Zhang, A. W. Young, M. Lebrat, and M. Greiner, *Nature* **642**, 909 (2025).
- [21] T. Chalopin, P. Bojović, S. Wang, T. Franz, A. Sinha, Z. Wang, D. Bourgund, J. Obermeyer, F. Grusdt, A. Bohrdt, L. Pollet, A. Wietek, A. Georges, T. Hilker, and I. Bloch, Probing the magnetic origin of the pseudogap using a fermi-hubbard quantum simulator (2024), arXiv:2412.17801 [cond-mat.str-el].
- [22] L. H. Kendrick, A. Kale, Y. Gang, A. D. Deters, M. Lebrat, A. W. Young, and M. Greiner, Pseudogap in a fermi-hubbard quantum simulator (2025), arXiv:2509.18075 [cond-mat.quant-gas].
- [23] A. M. Rey, R. Sensarma, S. Fölling, M. Greiner, E. Demler, and M. D. Lukin, *Europhysics Letters* **87**, 60001 (2009).
- [24] T. Kitagawa, A. Aspect, M. Greiner, and E. Demler, *Phys. Rev. Lett.* **106**, 115302 (2011).
- [25] A. F. Ho, M. A. Cazalilla, and T. Giamarchi, *Phys. Rev. A* **79**, 033620 (2009).
- [26] H. Schröder, H. Lange, T. Franz, T. Chalopin, P. Bojović, S. Wang, I. Bloch, T. A. Hilker, F. Grusdt, and A. Bohrdt, *PRX Quantum* **5**, 040341 (2024).
- [27] D. K. Mark, H.-Y. Hu, J. Kwan, C. Kokail, S. Choi, and S. F. Yelin, *Phys. Rev. Lett.* **135**, 123402 (2025).
- [28] H. Xu, C.-M. Chung, M. Qin, U. Schollwöck, S. R. White, and S. Zhang, *Science* **384**, eadh7691 (2024), <https://www.science.org/doi/pdf/10.1126/science.adh7691>.
- [29] P. T. Brown, E. Guardado-Sánchez, B. M. Spar, E. W. Huang, T. P. Devereaux, and W. S. Bakr, *Nature Physics* **16**, 26 (2020).
- [30] A. Bohrdt, E. Demler, F. Pollmann, M. Knap, and F. Grusdt, *Phys. Rev. B* **102**, 035139 (2020) 10.1103/PhysRevB.102.035139 (2020), 2001.05509.
- [31] I. M. Navarro, C. Weitenberg, K. Sengstock, and E. Demler, *SciPost Phys.* **16**, 081 (2024).
- [32] N. B. Jørgensen, L. Wacker, K. T. Skalmstang, M. M. Parish, J. Levinsen, R. S. Christensen, G. M. Bruun, and J. J. Arlt, *Phys. Rev. Lett.* **117**, 055302 (2016).
- [33] M. G. Skou, K. K. Nielsen, T. G. Skov, A. M. Morgen, N. B. Jørgensen, A. Camacho-Guardian, T. Pohl, G. M. Bruun, and J. J. Arlt, *Phys. Rev. Res.* **4**, 043093 (2022).
- [34] A. Damascelli, Z. Hussain, and Z.-X. Shen, *Rev. Mod. Phys.* **75**, 473 (2003).
- [35] J. A. Sobota, Y. He, and Z.-X. Shen, *Rev. Mod. Phys.* **93**, 025006 (2021).
- [36] T.-L. Dao, A. Georges, J. Dalibard, C. Salomon, and I. Carusotto, *Phys. Rev. Lett.* **98**, 240402 (2007).
- [37] T.-L. Dao, I. Carusotto, and A. Georges, *Phys. Rev. A* **80**, 023627 (2009).
- [38] C. Kollath, A. Iucci, T. Giamarchi, W. Hofstetter, and U. Schollwöck, *Phys. Rev. Lett.* **97**, 050402 (2006).
- [39] P. Torma, *Physica Scripta* **91**, 043006 (2016).
- [40] M. Cetina, M. Jag, R. S. Lous, I. Fritzsche, J. T. M. Walraven, R. Grimm, J. Levinsen, M. M. Parish, R. Schmidt, M. Knap, and E. Demler, *Science* **354**, 96 (2016).
- [41] L. A. Pena Ardila, N. B. Jørgensen, T. Pohl, S. Giorgini, G. M. Bruun, and J. J. Arlt, *Phys. Rev. A* **99**, 063607 (2019).
- [42] M. G. Skou, T. G. Skov, N. B. Jørgensen, K. K. Nielsen, A. Camacho-Guardian, T. Pohl, G. M. Bruun, and J. J. Arlt, *Nature Physics* **17**, 731 (2021).
- [43] J. Leonard, S. Kim, J. Kwan, P. Segura, F. Grusdt, C. Repellin, N. Goldman, and M. Greiner, *Nature* **619**, 495 (2023).
- [44] P. Lunt, P. Hill, J. Reiter, P. M. Preiss, M. Gałka, and S. Jochim, *Phys. Rev. Lett.* **133**, 253401 (2024).
- [45] B. Wang, X.-Y. Dong, and A. Eckardt, *SciPost Phys.* **12**, 095 (2022).
- [46] N. Read, *Phys. Rev. Lett.* **62**, 86 (1989).
- [47] F. Pauw, F. A. Palm, U. Schollwöck, A. Bohrdt, S. Paeckel, and F. Grusdt, *Phys. Rev. Res.* **6**, 023180 (2024).
- [48] C. Weitenberg, M. Endres, J. F. Sherson, M. Cheneau, P. Schauß, T. Fukuhara, I. Bloch, and S. Kuhr, *Nature* **471**, 319 (2011).

[49] L.-C. Ha, L. W. Clark, C. V. Parker, B. M. Anderson, and C. Chin, Phys. Rev. Lett. **114**, 055301 (2015).

[50] J. Koepsell, S. Hirthe, D. Bourgund, P. Sompel, J. Vijayan, G. Salomon, C. Gross, and I. Bloch, Phys. Rev. Lett. **125**, 010403 (2020).

[51] M. Horvath, S. Dhar, A. Das, M. D. Frye, Y. Guo, J. M. Hutson, M. Landini, and H.-C. Nägerl, Nature Communications **17**, 3739 (2024).

[52] M. Holten, L. Bayha, K. Subramanian, S. Brandstetter, C. Heintze, P. Lunt, P. M. Preiss, and S. Jochim, Nature **606**, 287 (2022).

[53] R. G. Hulet, J. H. V. Nguyen, and R. Senaratne, Review of Scientific Instruments **91**, 011101 (2020).

[54] B. Santra, C. Baals, R. Labouvie, A. B. Bhattacherjee, A. Pelster, and H. Ott, Nature Communications **8**, 1 (2017).

[55] S. Braun, J. P. Ronzheimer, M. Schreiber, S. S. Hodgman, T. Rom, I. Bloch, and U. Schneider, Science **339**, 52 (2013), <https://www.science.org/doi/pdf/10.1126/science.1227831>.

[56] C. W. von Keyserlingk, T. Rakovszky, F. Pollmann, and S. L. Sondhi, Phys. Rev. X **8**, 021013 (2018).

[57] P. Sierant, M. Lewenstein, A. Scardicchio, L. Vidmar, and J. Zakrzewski, Reports on Progress in Physics **88**, 026502 (2025).

[58] A. Defossez, L. Vanderstraeten, L. P. Gavensky, and N. Goldman, (2025), arXiv:2412.14886 [quant-ph].

[59] F. A. Palm, A. Imperietro, M. Aidelsburger, and N. Goldman, Extracting transport coefficients from local ground-state currents (2025), arXiv:2510.19742 [cond-mat.quant-gas].

[60] R. Islam, R. Ma, M. Preiss, Philipp M. Eric Tai, A. Lukin, M. Rispoli, and M. Greiner, Nature **528**, 77 (2015).